

DepthFM: Fast Monocular Depth Estimation with Flow Matching

Ming Gui*, Johannes S. Fischer*, Ulrich Prestel,
Pingchuan Ma, Dmytro Kotovenko, Olga Grebenkova,
Stefan Andreas Baumann, Vincent Tao Hu, and Björn Ommer

CompVis @ LMU Munich, MCML

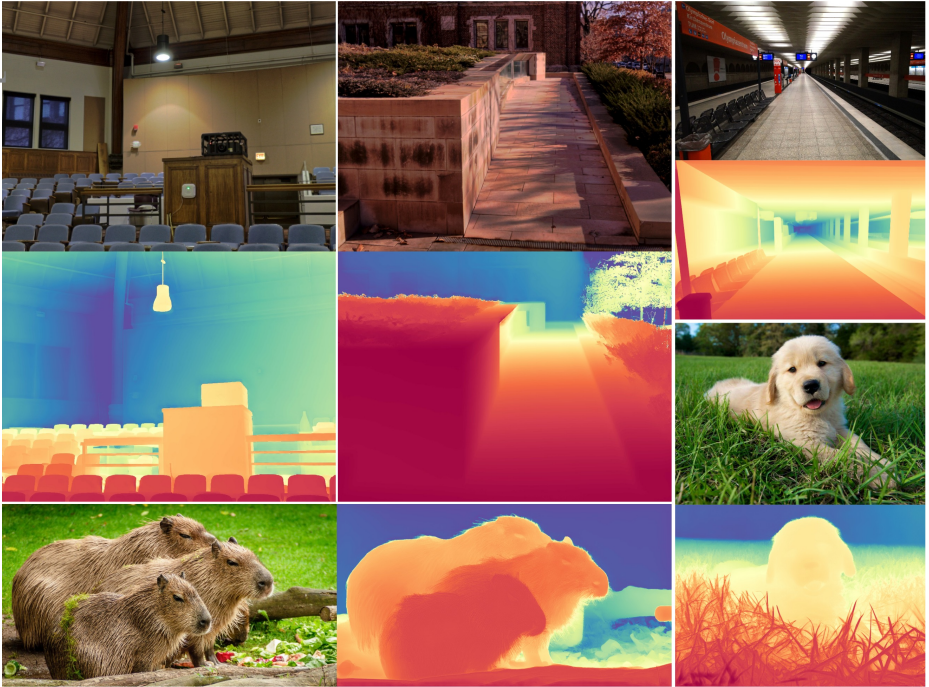


Fig. 1: We present DepthFM, a fast-inference flow matching model with strong zero-shot generalization capabilities. Fine-tuned from the foundation model SD2.1, our model can exploit the strong prior and readily generalize to unseen real images while being trained only on synthetic data.

Abstract. Monocular depth estimation is crucial for numerous downstream vision tasks and applications. Current discriminative approaches to this problem are limited due to blurry artifacts, while state-of-the-art generative methods suffer from slow sampling due to their SDE nature. Rather than starting from noise, we seek a direct mapping from input image to depth map. We observe that this can be effectively framed using

* Equal Contribution

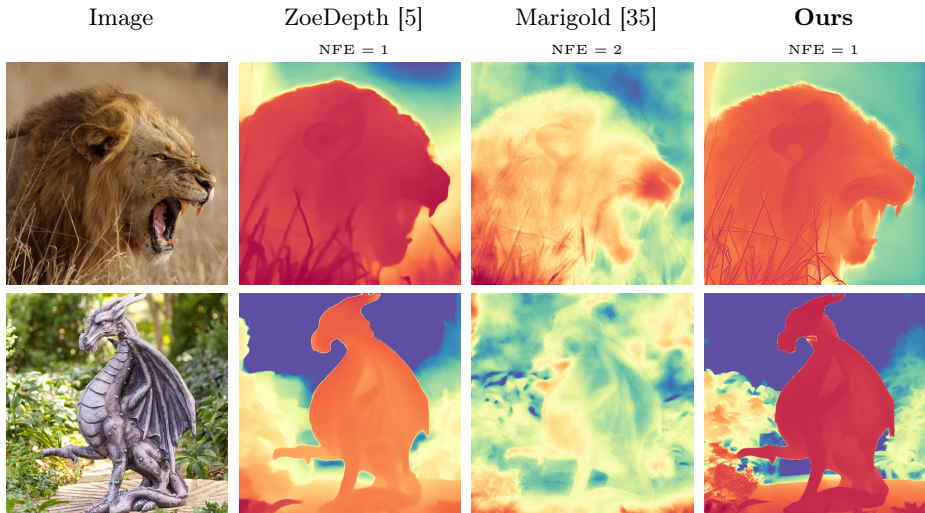


Fig. 2: We achieve significantly sharper images with just one function evaluation compared to other state-of-the-art models. The depth estimations from Marigold take twice as long as ours but fail to generate depth maps of the same granularity.

flow matching, since its straight trajectories through solution space offer efficiency and high quality. Our study demonstrates that a pre-trained image diffusion model can serve as an adequate prior for a flow matching depth model, allowing efficient training on only synthetic data to generalize to real images. We find that an auxiliary surface normals loss further improves the depth estimates. Due to the generative nature of our approach, our model reliably predicts the confidence of its depth estimates. On standard benchmarks of complex natural scenes, our lightweight approach exhibits state-of-the-art performance at favorable low computational cost despite only being trained on little synthetic data. Project page and code are available at <https://depthfm.github.io/>

Keywords: Depth Estimation · Flow Matching · Generative Model

1 Introduction

A key objective of computer vision is understanding our 3D surroundings, especially scene depth and surface orientation, from mere 2D images, since they are still constituting the most prevalent source of visual information. Monocular depth and surface normal estimation are pivotal due to their numerous applications, ranging from core vision tasks such as segmentation [23] and visual synthesis [79] to application areas like robotics and autonomous driving [7, 21].

Despite the recent strides in this field, estimating realistic geometry from a single image remains challenging. State-of-the-art discriminative depth estima-

tion models exhibit impressive performance overall but suffer from blurry edges and lack of fine-grained details due to their mode averaging behavior associated with MSE regression within the training paradigm. Marigold [35], a recent state-of-the-art generative approach based on diffusion models addresses this issue but suffers from extremely long inference times due to their reliance on solving stochastic differential equations.

To this end, flow matching models (FM) [1, 42, 43] comes as an attractive paradigm, as it is orthogonal to the currently prominent diffusion models (DM) [26, 66, 69]. While diffusion models offer samples of great diversity, the curved diffusion trajectories through solution space entail high computational costs. Conversely, the much straighter trajectories of flow matching entail much faster processing [38, 42]. We hypothesize that these characteristics of flow matching are a much better fit to the problems of depth and surface normal estimation from a single image than diffusion models. To further enhance the training and inference efficiency, we utilize data-dependent couplings for our DepthFM model, as detailed in Sec. 3.1. In contrast to conventional diffusion models that initiate the generative process from noise and conclude with a depth field, our method establishes direct relations between input image and depth.

To render training computationally feasible, we augment our model with prior information by finetuning our approach from an image synthesis foundation model, specifically, SD2.1 [57]. We show the feasibility of *transferring information between DM and FM* by finetuning a flow matching model from a diffusion model prior. This equips our model with initial visual cues and significantly speeds up training. This approach enables us to exclusively train on a small amount of *synthetic data*, yet achieve robust *generalization to real-world images*.

Notably, the use of synthetic data provides an additional advantage, as it often comes paired with ground truth surface normals. Leveraging this information, we can derive an auxiliary surface normal loss, where we compare the ground truth surface normal field to our predicted surface normal field derived from our depth predictions. Our findings demonstrate that incorporating this auxiliary loss enhances depth prediction and improves quantitative performance. Lastly, our generative approach also provides reliable confidence estimates of its predictions, allowing it to express uncertainty over depth estimates.

In summary, our contributions are as follows:

- We present *DepthFM*, a state-of-the-art, versatile, and fast monocular depth estimation model. Beyond conventional depth estimation tasks. DepthFM also demonstrates state-of-the-art capabilities in downstream tasks such as *depth inpainting* and *depth conditional image synthesis*.
- We demonstrate the successful transfer of the strong image prior from a diffusion model to a flow matching model with minimal reliance on training data and without the need for real-world images.
- We show that flow matching models are efficient and able to synthesize depth maps within a single inference step.

- DepthFM achieves outstanding performance on benchmark datasets and natural images, despite only being trained on synthetic data.
- We include a surface normal loss as an auxiliary objective to obtain more accurate depth estimates.
- Besides depth estimation, our approach also reliably predicts the confidence of its predictions.

2 Related Works

2.1 Depth Estimation

Depth Estimation is a common task in computer vision. It is usually approached in either a discriminative or a generative manner. For discriminative depth estimation, it can be categorized into regressing metric depth [3, 4, 34, 41, 45, 77] and relative depth [37, 45, 52, 54]. A common approach is to discretize the target depth interval and reformulate the continuous depth regression as a classification task [20, 39, 40, 55, 75].

Various approaches have emerged within the realm of generative models, particularly diffusion models [14, 33, 63, 81], which aims to leverage diffusion models for metric depth estimation. For instance, DDP [33] proposes an architecture to encode images but decode depth maps, achieving state-of-the-art results on the KITTI dataset. DepthGen [65] extends a multi-task diffusion model to metric depth prediction which also handles the noisy ground truth. Its successor, DDVM [63], emphasizes pretraining on synthetic and real data for enhanced depth estimation capabilities. Recently, diffusion-based Marigold [35] produces high-quality depth estimates but suffers from prolonged sampling times due to their reliance on solving stochastic differential equations (SDEs) [69]. The aforementioned SDE necessitates a Gaussian source distribution [66, 68], which may not always align with the natural correlation between images and depth maps. In contrast, flow matching-based models [1, 42, 43] have shown promise across various tasks and offers faster sampling speeds [28, 43]. Optimal transport between the source distribution can also be satisfied [70] when the source distribution deviates from a Gaussian distribution, which can be advantageous for certain tasks. We take the initiative step to explore integrating the principles of flow matching into the task of monocular depth estimation to minimize the sampling cost by leveraging the inherent straight sampling trajectory nature [38].

2.2 Diffusion and Flow Matching Models

Diffusion models [26, 66, 69] have excelled at various image generation tasks, including unconditional and class-conditional generation [13, 27, 30], image-to-image translation [59, 61], text-to-image synthesis [48, 51, 57, 60], and text-guided image editing [6, 24, 44, 72]. Additionally, they have been applied in discriminative tasks such as image enhancement [59], panoptic segmentation [9], and depth estimation [65]. On the other hand, flow-based methods like flow matching [1,

42, 43] have gained considerable attention and have been explored in various domains, including image generation [16, 28, 42], video prediction [12], human motion generation [29], point cloud generation [73], and manifold data generation [8]. However, to the best of our knowledge, no prior work has explored leveraging flow matching to facilitate the distribution shift between images and depth maps, despite their intuitive closeness in comparison to noise and depth maps.

3 Method

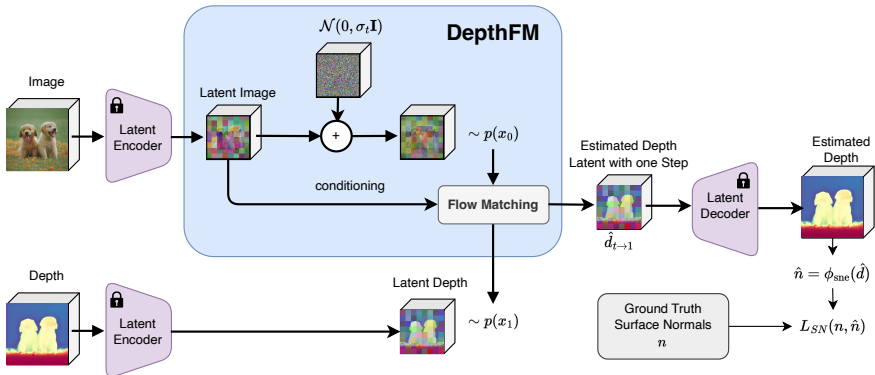


Fig. 3: Overview of our training pipeline. Our training is restricted by flow matching and surface normal loss. For flow matching, we use data-dependent flow matching to regress the vector field between the ground truth depth and the corresponding image. Additionally, we enforce geometric realism through a surface normal loss.

3.1 Flow Matching

Flow matching models [1, 42, 43] belong to the category of generative models designed to regress vector fields based on fixed conditional probability paths. Denote \mathbb{R}^d as the data space with data points x and $u_t(x) : [0, 1] \times \mathbb{R}^d \rightarrow \mathbb{R}^d$ the time-dependent vector field, which defines the ODE $dx = u_t(x)dt$. Here, $\phi_t(x)$ represents the solution to this ODE with the initial condition $\phi_0(x) = x$.

The probability density path $p_t : [0, 1] \times \mathbb{R}^d \rightarrow \mathbb{R}_{>0}$ characterizes the probability distribution of x at timestep t with $\int p_t(x)dx = 1$. The pushforward function $p_t = [\phi_t]_{\#}(p_0)$ then transports the probability density path p along u from timestep 0 to t .

Lipman et al. [42] showed that we can acquire the same gradients and therefore efficiently regress the neural network using the conditional flow matching objective, where we can compute $u_t(x|z)$ by efficiently sampling $p_t(x|z)$,

$$\mathcal{L}_{FM}(\theta) = \mathbb{E}_{t,q(z),p_t(x|z)} \|v_{\theta}(t, x) - u_t(x|z)\|, \quad (1)$$

with z as a conditioning variable and $q(z)$ the distribution of that variable. We parameterize v_θ as a U-Net [58], which takes the data sample x as input and z as conditioning information.

Latent Flow Matching In order to reduce the computational demands associated with training FM models for high-resolution depth estimation synthesis, we follow [11, 18, 31, 57] and utilize an autoencoder model that provides a compressed latent space that aligns perceptually with the image pixel space. This approach also facilitates the direct inheritance of a robust model prior obtained from foundational LDMs such as Stable Diffusion. We move all modalities (i.e., RGB images, depths, and surface normals) to the latent space. Please refer to Sec. 3.2 for more details.

Data Dependent Flow Matching Given access to image-to-depth pairs, we incorporate the intrinsic relationship between the conditioning signal of the image and the target depth field. While prior works focus on the relationship within the same modality (images) [1, 18], we explore the integration of terminal distributions of different modalities.

In our approach, x_1 represents encoded depth samples in the latent space, and the starting point x_0 corresponds to an encoded representation of the corresponding image. We smooth around the data samples within a minimal variance to acquire the corresponding data distribution $\mathcal{N}(x_0, \sigma_{\min}^2)$ and $\mathcal{N}(x_1, \sigma_{\min}^2)$. The Gaussian flows can be defined by the equations

$$p_t(x|z) = \mathcal{N}(x|tx_1 + (1-t)x_0, \sigma_{\min}^2 \mathbf{I}), \quad (2)$$

$$u_t(x|z) = x_1 - x_0, \quad (3)$$

$$\phi_t(x|z) = tx_1 + (1-t)x_0. \quad (4)$$

Despite the different modalities and data manifolds of x_0 and x_1 , the optimal transport condition between $p(x_0)$ and $p(x_1)$ is inherently satisfied due to image-to-depth pairs. This addresses the dynamic optimal transport problem in the transition for image-to-depth translation within the flow matching paradigm, ensuring more stable and faster training [70]. The loss in this setting takes the form of:

$$\mathcal{L}_{FM}(\theta) = \mathbb{E}_{t,z,p(x_0)} \|v_\theta(t, \phi_t(x_0)) - (x_1 - x_0)\|. \quad (5)$$

Noise Augmentation Noise augmentation is a technique for boosting generative models' performance first introduced for cascaded diffusion models [27]. The authors found that applying random Gaussian noise or Gaussian blur to the conditioning signal in super-resolution diffusion models results in higher-quality

results during inference. Drawing inspiration from this, we also implement Gaussian noise augmentation on x_0 . Following the notation from variance-preserving DMs, we noise x_0 according to the cosine schedule first proposed in [47]. In line with [18, 27], we empirically discover in our experiments that incorporating a specific amount of Gaussian noise enhances performance. We hypothesize that including a small amount of Gaussian noise smoothes the base probability density p_0 so that it remains well-defined over a wider manifold. Note that this noise augmentation is only applied to x_0 but not to the conditioning information z since the model relies on the precise conditioning information to construct the straight path.

Finetuning FM from DM prior Diffusion models are a class of generative models that can be adapted to various parameterizations, including the x , ϵ , and v parameterizations. In particular, the v parameterization is characterized by regressing the "velocity" between samples from the two terminal distributions [62]. In the context of FM, where the two terminal distribution samples are denoted as x_0 and x_1 , the objective of the v parameterization could be mathematically formulated as $v = \alpha_t x_0 - \sigma_t x_1$, where α_t and σ_t are the fixed diffusion schedule. Our FM objective regresses a vector field of $v = x_1 - x_0$. The similarity reveals a correlation between the DM and FM objectives. Consequently, we can fine-tune our FM model directly from the v -parameterized SD2.1 checkpoint and achieve good performance with little training. We have also tried to post-hoc transform the SD model output into the FM objective, but this modification did not lead to improved empirical results.

The SD2.1 checkpoint is not directly compatible with our FM model, since our model requires an additional ground truth image for conditioning. To address this, we modify our model by expanding and duplicating the first convolution layer weights to ensure compatibility. We also tune down the weights of that layer to preserve the input magnitude to the subsequent layer. We deactivate text conditioning and employ null-text embedding as the input for cross-attention.

3.2 Depth Normalization

Inspired by [35], we convert the depth images into three channels to simulate an RGB image. We also find that the data range is essential for the performance of the latent encoder. While images can be normalized quite easily and surface normals lie naturally within the range of [-1,1], we need to normalize the depth images also to the value range of [-1, 1]. Similar to [35], we compute the quantiles of the individual datasets and normalize them individually. The normalization process can then be depicted as

$$\tilde{d} = \left(\frac{\mathbf{Fn}(d) - \mathbf{Fn}(d_2)}{\mathbf{Fn}(d_{98}) - \mathbf{Fn}(d_2)} - 0.5 \right) \cdot 2, \quad (6)$$

where d_2 and d_{98} correspond to the 2% and the 98% quantile of the dataset, and \mathbf{Fn} is the normalization function, where we can use the identity function,

log function, inverse function, etc. After this normalization function, we pass it through the encoder and obtain the corresponding latent representations. We provide a more in-depth explanation in Sec. A.3.

3.3 Surface Normal Loss

During training, we sample x_t from $p(x_t|x_0, x_1)$ for $t \in [0, 1]$ and then use our model to regress the vector field v_t that pushes x_t in the direction of x_1 , which represents the depth map in our case. Due to the straight trajectories enforced through flow matching method, we obtain accurate estimates of the final depth map with just one number of function evaluations (NFE) (see Fig. 4). Consequently, we can geometrically constrain our model with an auxiliary surface normals loss. Starting from x_t we obtain an estimate of the final latent code $\hat{x}_{t \rightarrow 1}$ using v_t , which we decode with the pre-trained autoencoder to obtain an estimate of the depth \hat{d} . Based on \hat{d} we can estimate the surface normals \hat{n} using a surface-normal estimator $\phi_{\text{sne}}(d)$. For ϕ_{sne} we choose a purely geometry-based estimator, which utilizes the fact that the normals can be constructed via the gradient of the depth [17, 19], and can therefore be used as an additional training-signal. Furthermore, it is known, that the error for this type of surface-normal estimator is the greatest on edges [17]. Therefore, to reduce noisy learning signals during training, we apply a confidence mask $\mathcal{M}(n)$, which we obtain using a simple edge detection filter applied on the ground truth surface normals. Given the ground truth normals n , the estimated depth \hat{d} at time t , the confidence mask $\mathcal{M}(n)$, and the surface-normal estimator ϕ_{sne} we define the surface-normal loss as

$$\mathcal{L}_{\text{SN}}(n, \hat{n}, t) = \pi(t)\psi(n \odot \mathcal{M}(n), \phi_{\text{sne}}(\hat{d}) \odot \mathcal{M}(n)) \quad (7)$$

where $\psi(\cdot, \cdot)$ is a distance measure between surface normals and $\pi(t)$ defines a weighting schedule of the surface normals loss, and \odot denotes the element-wise product. We include the surface-normal loss as a form of surface-regularization. Given that one-step estimates from earlier time steps t may be less precise, we reduce their influence on the final loss while enhancing the contribution of later time steps. In the experiments section we ablate different design choices of distance measure $\psi(\cdot, \cdot)$ and weighting schedule $\pi(t)$.

3.4 Final Loss

Combining the two previously mentioned parts of the loss, we can define our final training loss as a combination of the data-dependent flow matching objective and the surface normals loss:

$$\mathcal{L} = \mathcal{L}_{\text{FM}} + \lambda\mathcal{L}_{\text{SN}}, \quad (8)$$

where λ is a weighting factor for the surface normals loss.

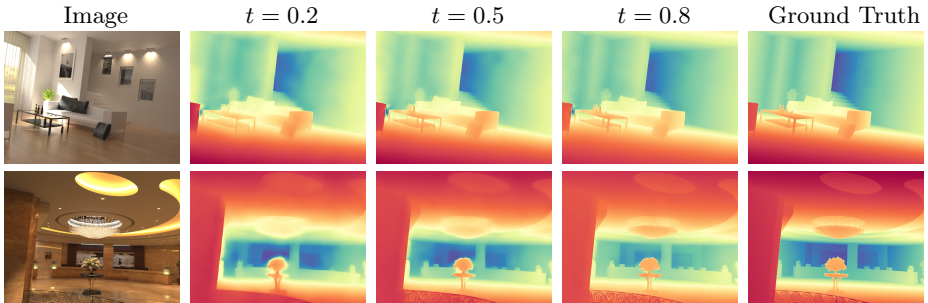


Fig. 4: Single ODE step inference results of our model after 5k training iterations from different x_t . Samples from Hypersim validation split [56].

4 Experiments

4.1 Dataset and Metrics

We train our depth estimation model on two synthetic datasets, Hypersim [56] and Virtual KITTI [7]. To comprehensively evaluate its performance and demonstrate our model’s strong generalization capabilities, we conduct zero-shot evaluations on well-established real-world datasets e.g., NYUv2 [46], KITTI [2] and DIODE [71]. We denote the ground truth depth as d and the depth prediction as \hat{d} . The assessment metrics are then the Absolute Mean Relative Error (RelAbs), calculated as $\frac{1}{M} \sum_{i=1}^M |d_i - \hat{d}_i|/d_i$ and the $\delta 1$ accuracy which measures the ratio of all pixels satisfying $\max(d_i/\hat{d}_i, \hat{d}_i/d_i) < 1.25$.

Since our model is purely trained on synthetic data, we adopt the affine-invariant loss to ignore the scale and shift of each unknown sample at evaluation. We do a least squares fit of scale and shift to our model’s prediction d^* in the corresponding normalization space to minimize the MSE so that $\hat{d} = \frac{d^* - t(d^*)}{s(d^*)}$. In our ensembling approach, we individually apply scale and shift operations to each depth estimation. Subsequently, we obtain the final prediction by computing a simple average across all the individually transformed predictions.

We find that applying the log function yields the best performance and alleviates the range difference between indoor and outdoor datasets. We further ablate this choice in Sec. A.3.

4.2 Zero-shot Depth Estimation

Our model exhibits remarkable generalization capabilities by only training on 63k purely synthetic samples and is capable of *zero-shot* depth estimation across both indoor and outdoor datasets. Tab. 1 qualitatively demonstrates our performance against state-of-the-art counterpart models. While other models often rely on extensive datasets for training, we leverage the rich knowledge inherent

Table 1: Qualitative comparison of DepthFM with SOTA affine-invariant depth estimators on **zero-shot** benchmarks. $\delta 1$ is presented in percentage. Our method outperforms other methods across the datasets in most cases. Most baselines are sourced from Metric3D [74] and Marigold [35]. For Marigold (*) we conducted a grid search over NFEs and ensemble numbers, with the reported metric corresponding to the optimal combination.

Method	#Training samples		NYUv2		KITTI		DIODE	
	Real	Synthetic	AbsRel↓	$\delta 1$ ↑	AbsRel↓	$\delta 1$ ↑	AbsRel↓	$\delta 1$ ↑
MiDaS [54]	2M	—	0.111	88.5	0.236	63.0	0.332	71.5
Omnidata [15]	11.9M	301K	0.074	94.5	0.149	83.5	0.339	74.2
HDN [78]	300K	—	0.069	94.8	0.115	86.7	0.246	78.0
DPT [53]	1.2M	188K	0.098	90.3	0.100	90.1	0.182	75.8
Marigold* [35]	—	74K	0.061	<u>94.9</u>	<u>0.099</u>	<u>91.6</u>	0.275	<u>78.5</u>
Naïve FM	—	63K	0.076	94.1	0.100	91.4	0.233	78.4
DepthFM (<i>ours</i>)	—	63K	<u>0.065</u>	95.6	0.083	93.4	<u>0.225</u>	80.0

in a diffusion-based foundation model. This approach not only conserves computational resources but also emphasizes the adaptability and training efficiency of our model.

Comparisons against Generative Models Our DepthFM model showcases remarkable sampling speed without compromising performance. To highlight the inference efficiency of our proposed model, we conduct a quantitative evaluation against Marigold [35], a representative diffusion-based generative model. Note that we finetune from the same foundation image synthesis model (SD2.1) and share the network architecture [57]. We show quantitative evaluation results against the diffusion-based Marigold [35] model in the low number of function evaluations (NFE) regime in Fig. 5. Our model with *one* NFE consistently outperforms Marigold at *four* NFEs and maintains superior results across varying NFEs. This is also confirmed qualitatively in Fig. 6. While Marigold requires at least two function evaluations, we can achieve very good results with only one function evaluation. These experiments empirically demonstrate the effectiveness of our DepthFM model with straight trajectories when compared to its diffusion-based counterpart. Marigold uses ensembling techniques to further improve depth estimation. We find that this also improves performance in our case, as visualized in Fig. 9.

Comparisons against Discriminative Models Blurry lines at object edges are a common problem in depth estimation, making downstream tasks such as 3D warping difficult. Our generative solution remedies this problem, resulting in sharper and crisper depth predictions, as visualized in Fig. 2. This improvement has significant implications for the robustness of our model in scenarios where accurate depth information is paramount.

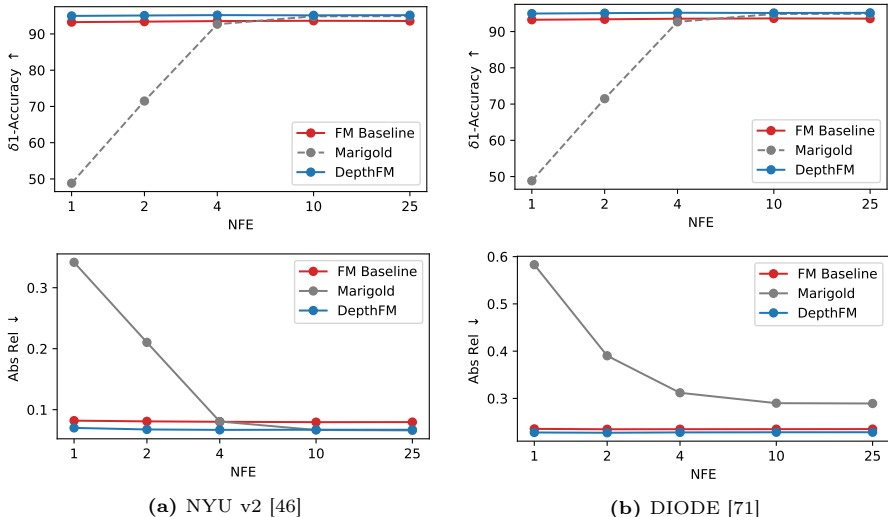


Fig. 5: Comparison of the diffusion-based *Marigold* [35] depth estimation, a *Flow Matching (FM) Baseline*, and our *DepthFM* model. Each method is evaluated with only one ensemble member and for different number of function evaluations (NFE) on two common benchmark datasets. We evaluate Marigold based on their official repository. In contrast to the FM baseline, DepthFM incorporates our proposed improvements, such as normals loss and data-dependent coupling during training.

Another distinctive feature of our DepthFM model lies in its inherent ability to provide confidence estimates along with depth predictions, which stems from the stochastic nature embedded within the generative training paradigm. Unlike discriminative models, our generative approach enables the quantification of uncertainty for each depth prediction. Please refer to Sec. 4.4 for more details.

Generalization across Resolutions Fig. 11 shows a collection of images with varying resolutions and aspect ratios. Even though our model was only trained on synthetic data on a fixed resolution of 384×512 pixels, it generalizes surprisingly well to real data with different resolutions and aspect ratios while producing realistic depth maps.

4.3 Depth Completion

An important task related to depth estimation is depth completion. Due to the hardware limitations of depth sensors, only a partial depth image is available. Therefore, the task is to fill in the rest of the missing depth values with the most plausible depth estimate. We finetune our model on synthetically generated partial depth maps, where only 2% of pixels are available. In order to pass the sparse depth and its corresponding mask into the autoencoder, while losing as little information as possible, we first create a dense representation via nearest-neighbor interpolation and distance-functions respectively. More concretely, to represent the depth-mask for a pixel p , we store the value $\min_{p' \in \mathcal{M}} \|p' - p\|_2$,

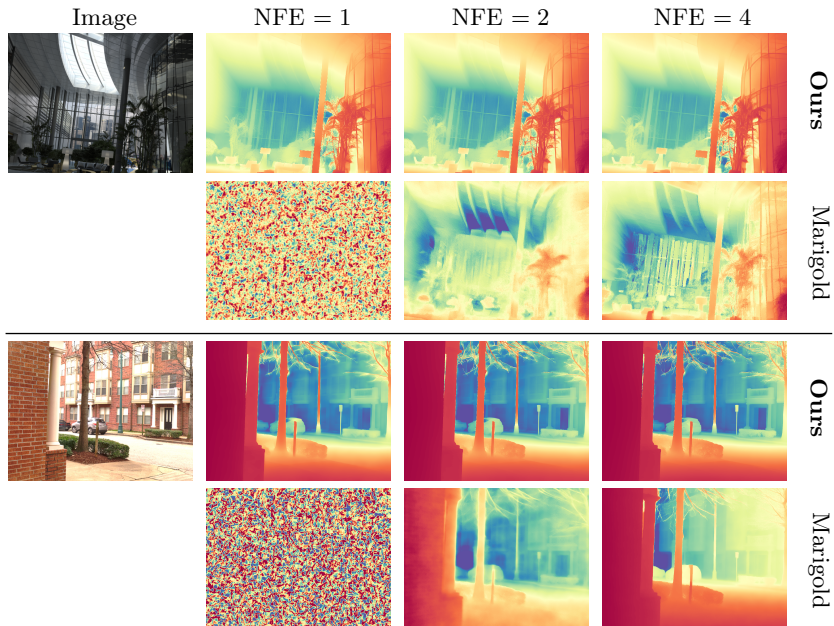


Fig. 6: Qualitative results for *Marigold* [35] vs our DepthFM model for different number of function evaluations. Note that with one-step inference Marigold does not give any meaningful results, whereas ours already shows realistic depth maps.

where \mathcal{M} is the mask. We fine-tune our monocular depth estimation model first for 10k steps on Hypersim [56] and then 8k more steps on NYU-v2 [46] on a depth-completion task, where we further inflate the first convolutional layer to accept extra conditionings including sparse depth and sparse depth mask. Given that the autoencoder is designed to handle non-sparse data, we upsample the sparse depth data using nearest neighbor interpolation and upsample the sparse depth mask using its distance function with l_2 -norm. Training parameters are the same as for our normal model training described in Sec. A.4. During training and evaluation, only 2 % of ground-truth pixels are available. Tab. 2 shows that with minimal fine-tuning our DepthFM model can achieve state-of-the-art results on depth completion on the NYU-v2 dataset [46]. We provide additional zero-shot results on depth completion in Fig. 8 and evaluation-samples in Fig. 7.

Table 2: Comparison to SOTA baselines in the depth-completion task on NYUv2 [46].

	NLSPN [49]	DSN [50]	Struct-MDC [32]	CompletionFormer [80]	Ours
RMSE↓	0.092	0.102	0.245	0.09	0.0774

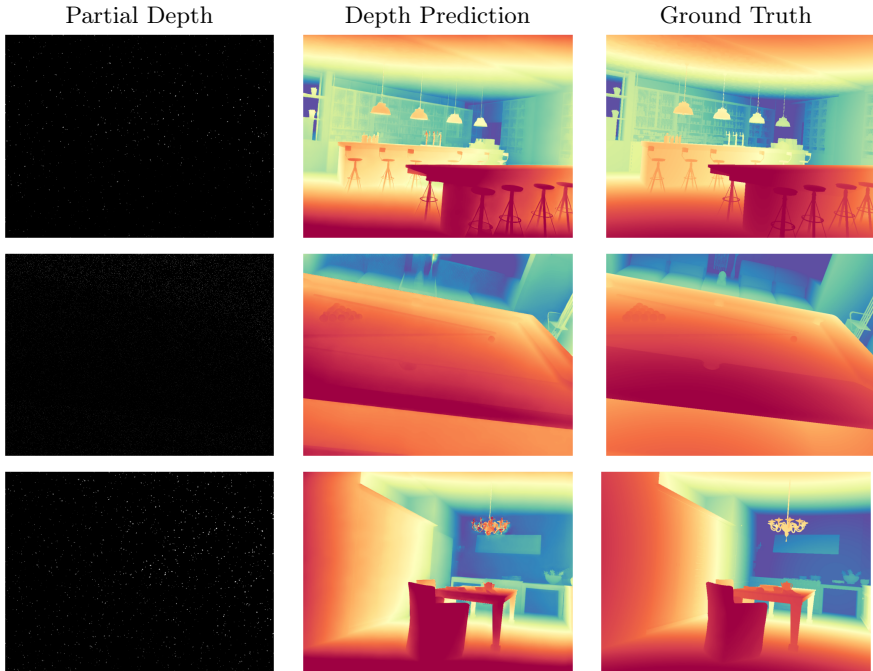


Fig. 7: Depth completion on Hypersim. *Left:* Given partial depth. *Middle:* Depth-estimate from the given partial depth. *Right:* Ground-truth depth.

4.4 Confidence Estimation

A major advantage of generative models is their ability to conditionally sample multiple times. Apart from improving overall performance, ensembling also provides a robust method for quantifying the confidence, or uncalibrated uncertainty, of the model. We estimate the uncalibrated uncertainty by calculating the standard deviation of the predictions over n_{ens} ensemble members. A higher standard deviation implies that the model’s predictions are less consistent and more sensitive to the stochasticity present in our DepthFM model. Fig. 10 shows an example image along with its corresponding depth estimate and uncalibrated uncertainty. The ensemble members show noticeable differences, especially in the high-frequency regions. Given the high frequency in these regions with drastic depth contrasts, these differences highlight the effectiveness of using ensembling with our model to measure the uncertainty of its predictions.

4.5 Ablations

Starting Distribution First, we compare our DepthFM to naïve FM. Similar to our method, naïve FM uses an optimal transport-based objective to regress vector fields but starts from Gaussian noise with $p(x_0) \sim \mathcal{N}(0, \mathbb{I})$. In contrast, our method starts from the latent code of the input image. Both models are provided



Fig. 8: Zero-shot depth completion on the NYU-v2 dataset [46]. The middle column is the ground truth raw depth, and the rightmost column is our depth prediction.

with the image as conditioning information over the full ODE trajectory. In our case, we have guaranteed optimal transport during training, which makes our method particularly training efficient. We evaluate both methods on the indoor and outdoor dataset DIODE [71] and the indoor dataset NYUv2 [46]. The results are visualized in Fig. 5 and clearly show that our DepthFM outperforms naïve Flow matching.

Auxiliary Normals Loss Next, we conduct an ablation study over the auxiliary surface normals loss. To ensure that the predicted depth maps are already well-defined, we first train our model for $20k$ iterations without surface normals loss and then fine-tune it with our auxiliary surface normals loss. We weigh the surface normals loss according to the timestep t from which we start our one-step push forward. We choose a cosine schedule emphasizing the loss from later timesteps (see Fig. 19 for a visualization). We define the starting point for the surface normals loss as t_s so that $\pi(t \leq t_s) = 0$ and $\pi(t = 1) = 1$. We find empirically that $t_s = 0.2$ works best, as shown in Tab. 3. We additionally ablate different configurations for $\phi(\cdot, \cdot)$ with $t_s = 0.2$. We observe that the normal consistency loss [15, 76], a combination of L1 and cosine loss $\phi(\hat{n}, n) = \|\hat{n} - n\|_1 + \|1 - \hat{n}^\top n\|_1$ gives the best results.

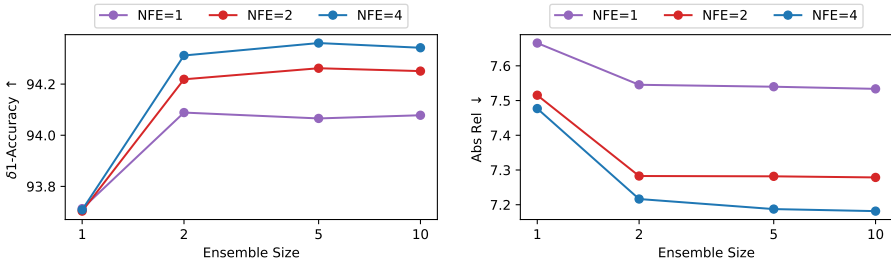


Fig. 9: Ablation of ensemble size for different number of function evaluations (NFE) on the NYU-v2 [46] dataset.

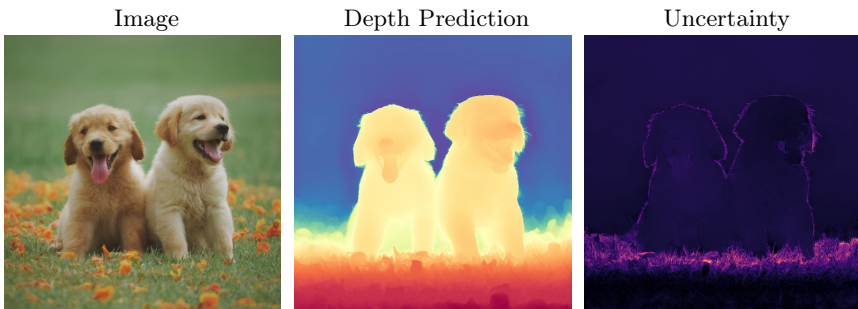


Fig. 10: *Left:* Original image. *Middle:* Mean depth prediction over 10 ensemble members. *Right:* Standard deviation as an indicator of uncalibrated uncertainty.

5 Conclusion

We present DepthFM, a flow matching approach for monocular depth estimation. By learning a direct mapping between input image and depth rather than denoising a normal distribution into a depth map, our approach is significantly more efficient than current diffusion-based solutions, while still providing fine-grained depth maps, without the common artifacts of discriminative paradigms. Our approach uses a pre-trained diffusion model for images as prior, which is effectively transferred to our flow matching model for depth. As a result, DepthFM has been trained only on synthetic data and still generalizes well to natural im-

Table 3: Ablation of the SN loss starting threshold. The experiments are conducted using $L2$ loss to determine the optimal starting threshold. With relatively consistent impact, we select the best configuration with $t_s = 0.2$.

	NYUv2				DIODE			
	None	$t_s = 0.0$	$t_s = 0.2$	$t_s = 0.5$	None	$t_s = 0.0$	$t_s = 0.2$	$t_s = 0.5$
$\delta 1 \uparrow$	93.4	93.3	93.8	93.4	78.5	78.5	78.7	78.6
AbsRel \downarrow	0.069	0.071	0.071	0.070	0.226	0.226	0.227	0.228

Table 4: Ablation of the surface normal auxiliary loss. Applying the normal consistency loss [15] best improves the model overall in terms of metrics.

	NYUv2					DIODE				
	None	L1	L2	Cosine	Normal	None	L1	L2	Cosine	Normal
$\delta \uparrow$	93.4	93.8	93.3	93.8	94.0	78.5	78.9	78.6	78.8	79.1
AbsRel \downarrow	0.069	0.070	0.070	0.069	0.068	0.226	0.226	0.228	0.226	0.228

ages during inference. In addition, an auxiliary surface normal loss has been shown to improve depth estimation. Our lightweight approach is competitive, fast, and provides reliable confidence estimates.

Acknowledgement

This project has been supported by the German Federal Ministry for Economic Affairs and Climate Action within the project “NXT GEN AI METHODS – Generative Methoden für Perzeption, Prädiktion und Planung”, the German Research Foundation (DFG) project 421703927, and the bidt project KLIMA-MEMES. The authors acknowledge the Gauss Center for Supercomputing for providing compute through the NIC on JUWELS at JSC.

References

- Albergo, M.S., Goldstein, M., Boffi, N.M., Ranganath, R., Vanden-Eijnden, E.: Stochastic interpolants with data-dependent couplings. arXiv (2023)
- Behley, J., Garbade, M., Milioto, A., Quenzel, J., Behnke, S., Stachniss, C., Gall, J.: Semantickitti: A dataset for semantic scene understanding of lidar sequences. In: ICCV (2019)
- Bhat, S.F., Alhashim, I., Wonka, P.: Adabins: Depth estimation using adaptive bins. In: CVPR (2021)
- Bhat, S.F., Alhashim, I., Wonka, P.: Localbins: Improving depth estimation by learning local distributions. In: ECCV (2022)
- Bhat, S.F., Birkl, R., Wofk, D., Wonka, P., Müller, M.: ZoeDepth: Zero-shot transfer by combining relative and metric depth. arXiv (2023)
- Brooks, T., Holynski, A., Efros, A.A.: Instructpix2pix: Learning to follow image editing instructions. arXiv (2022)
- Cabon, Y., Murray, N., Humenberger, M.: Virtual kitti 2 (2020)
- Chen, R.T., Lipman, Y.: Riemannian flow matching on general geometries. arXiv (2023)
- Chen, T., Li, L., Saxena, S., Hinton, G., Fleet, D.J.: A generalist framework for panoptic segmentation of images and videos. arXiv (2022)
- Cho, J., Min, D., Kim, Y., Sohn, K.: Diml/cvl rgb-d dataset: 2m rgb-d images of natural indoor and outdoor scenes (2021)
- Dao, Q., Phung, H., Nguyen, B., Tran, A.: Flow matching in latent space. arXiv (2023)

12. Davtayan, A., Sameni, S., Favaro, P.: Randomized conditional flow matching for video prediction. *arXiv* (2022)
13. Dhariwal, P., Nichol, A.: Diffusion models beat GANs on image synthesis. In: *NeurIPS* (2022)
14. Duan, Y., Guo, X., Zhu, Z.: DiffusionDepth: Diffusion denoising approach for monocular depth estimation. *arXiv* (2023)
15. Eftekhari, A., Sax, A., Malik, J., Zamir, A.: Omnidata: A scalable pipeline for making multi-task mid-level vision datasets from 3d scans. In: *ICCV*. pp. 10786–10796 (2021)
16. Esser, P., Kulal, S., Blattmann, A., Entezari, R., Müller, J., Saini, H., Levi, Y., Lorenz, D., Sauer, A., Boesel, F., et al.: Scaling rectified flow transformers for high-resolution image synthesis. *arXiv preprint arXiv:2403.03206* (2024)
17. Fan, R., Wang, H., Xue, B., Huang, H., Wang, Y., Liu, M., Pitas, I.: Three-filters-to-normal: An accurate and ultrafast surface normal estimator. *IEEE Robotics and Automation Letters* (2021)
18. Fischer, J.S., Gui, M., Ma, P., Stracke, N., Baumann, S.A., Ommer, B.: Boosting latent diffusion with flow matching. *arXiv* (2023)
19. Forsyth, D.A., Ponce, J.: *Computer Vision - A Modern Approach, Second Edition*. Pitman (2012)
20. Fu, H., Gong, M., Wang, C., Batmanghelich, N., Tao, D.: Deep ordinal regression network for monocular depth estimation. *CVPR* (2018)
21. Geiger, A., Lenz, P., Stiller, C., Urtasun, R.: Vision meets robotics: The kitti dataset. *The International Journal of Robotics Research* **32**(11), 1231–1237 (2013)
22. Guizilini, V., Ambrus, R., Pillai, S., Raventos, A., Gaidon, A.: 3d packing for self-supervised monocular depth estimation. In: *CVPR* (2020)
23. He, L., Lu, J., Wang, G., Song, S., Zhou, J.: Sosp-net: Joint semantic object segmentation and depth estimation from monocular images. *Neurocomputing* (2021)
24. Hertz, A., Mokady, R., Tenenbaum, J., Aberman, K., Pritch, Y., Cohen-Or, D.: Prompt-to-prompt image editing with cross attention control. *arXiv* (2022)
25. Hinterstoisser, S., Cagniart, C., Ilic, S., Sturm, P., Navab, N., Fua, P., Lepetit, V., Lepetit, b.: Gradient response maps for real-time detection of texture-less objects. *PAMI* (2012)
26. Ho, J., Jain, A., Abbeel, P.: Denoising Diffusion Probabilistic Models. *NeurIPS* (2020)
27. Ho, J., Saharia, C., Chan, W., Fleet, D.J., Norouzi, M., Salimans, T.: Cascaded diffusion models for high fidelity image generation. *JMLR* (2022)
28. Hu, V.T., Chen, Y., Caron, M., Asano, Y.M., Snoek, C.G., Ommer, B.: Guided diffusion from self-supervised diffusion features. In: *ARXIV* (2023)
29. Hu, V.T., Yin, W., Ma, P., Chen, Y., Fernando, B., Asano, Y.M., Gavves, E., Mettes, P., Ommer, B., Snoek, C.G.: Motion flow matching for human motion synthesis and editing. In: *ARXIV* (2023)
30. Hu, V.T., Zhang, D.W., Asano, Y.M., Burghouts, G.J., Snoek, C.G.M.: Self-guided diffusion models. In: *CVPR* (2023)
31. Hu, V.T., Zhang, D.W., Mettes, P., Tang, M., Zhao, D., Snoek, C.G.: Latent space editing in transformer-based flow matching. In: *ICML 2023 Workshop, New Frontiers in Learning, Control, and Dynamical Systems* (2023)
32. Jeon, J., Lim, H., Seo, D.U., Myung, H.: Struct-mdc: Mesh-refined unsupervised depth completion leveraging structural regularities from visual slam (2022)
33. Ji, Y., Chen, Z., Xie, E., Hong, L., Liu, X., Liu, Z., Lu, T., Li, Z., Luo, P.: DDP: Diffusion model for dense visual prediction. In: *ICCV* (2023)

34. Jun, J., Lee, J.H., Lee, C., Kim, C.S.: Depth map decomposition for monocular depth estimation. *arXiv* (2022)
35. Ke, B., Obukhov, A., Huang, S., Metzger, N., Dautt, R.C., Schindler, K.: Repurposing diffusion-based image generators for monocular depth estimation. In: *CVPR* (2024)
36. Koch, T., Liebel, L., Körner, M., Fraundorfer, F.: Comparison of monocular depth estimation methods using geometrically relevant metrics on the ibims-1 dataset. *Computer Vision and Image Understanding (CVIU)* (2020)
37. Lee, J.H., Kim, C.S.: Monocular depth estimation using relative depth maps. In: *CVPR* (2019)
38. Lee, S., Kim, B., Ye, J.C.: Minimizing trajectory curvature of ode-based generative models. *ICML* (2023)
39. Li, B., Dai, Y., He, M.: Monocular depth estimation with hierarchical fusion of dilated cnns and soft-weighted-sum inference. *Pattern Recognition* (2018)
40. Li, R., Xian, K., Shen, C., Cao, Z., Lu, H., Hang, L.: Deep attention-based classification network for robust depth prediction. In: Jawahar, C., Li, H., Mori, G., Schindler, K. (eds.) *ACCV* (2019)
41. Li, Z., Wang, X., Liu, X., Jiang, J.: Binsformer: Revisiting adaptive bins for monocular depth estimation. *arXiv* (2022)
42. Lipman, Y., Chen, R.T., Ben-Hamu, H., Nickel, M., Le, M.: Flow matching for generative modeling. *ICLR* (2023)
43. Liu, X., Gong, C., Liu, Q.: Flow straight and fast: Learning to generate and transfer data with rectified flow. *ICLR* (2023)
44. Meng, C., He, Y., Song, Y., Song, J., Wu, J., Zhu, J.Y., Ermon, S.: Sdedit: Guided image synthesis and editing with stochastic differential equations. In: *ICLR* (2021)
45. Mertan, A., Duff, D.J., Unal, G.: Single image depth estimation: An overview. *Digital Signal Processing* (2022)
46. Nathan Silberman, Derek Hoiem, P.K., Fergus, R.: Indoor segmentation and support inference from rgb-d images. In: *ECCV* (2012)
47. Nichol, A., Dhariwal, P.: Improved denoising diffusion probabilistic models. *arXiv* (2021)
48. Nichol, A., Dhariwal, P., Ramesh, A., Shyam, P., Pamela Mishkin, B.M., Sutskever, I., Chen, M.: GLIDE: Towards Photorealistic Image Generation and Editing with Text-Guided Diffusion Models. *arXiv* (2021)
49. Park, J., Joo, K., Hu, Z., Liu, C.K., Kweon, I.S.: Non-local spatial propagation network for depth completion. In: *ECCV* (2020)
50. de Queiroz Mendes, R., Ribeiro, E.G., dos Santos Rosa, N., Grassi, V.: On deep learning techniques to boost monocular depth estimation for autonomous navigation. *Robotics and Autonomous Systems* (2021)
51. Ramesh, A., Dhariwal, P., Nichol, A., Chu, C., Chen, M.: Hierarchical text-conditional image generation with clip latents. *arXiv* (2022)
52. Ranftl, R., Bochkovskiy, A., Koltun, V.: Vision transformers for dense prediction. In: *ICCV* (2021)
53. Ranftl, R., Bochkovskiy, A., Koltun, V.: Vision transformers for dense prediction. In: *ICCV* (2021)
54. Ranftl, R., Lasinger, K., Hafner, D., Schindler, K., Koltun, V.: Towards robust monocular depth estimation: Mixing datasets for zero-shot cross-dataset transfer. *TPAMI* (2020)
55. Ren, H., El-Khamy, M., Lee, J.: Deep robust single image depth estimation neural network using scene understanding. In: *CVPR Workshops* (2019)

56. Roberts, M., Ramapuram, J., Ranjan, A., Kumar, A., Bautista, M.A., Paczan, N., Webb, R., Susskind, J.M.: Hypersim: A photorealistic synthetic dataset for holistic indoor scene understanding. In: ICCV (2021)
57. Rombach, R., Blattmann, A., Lorenz, D., Esser, P., Ommer, B.: High-resolution image synthesis with latent diffusion models. In: CVPR (2022)
58. Ronneberger, O., Fischer, P., Brox, T.: U-net: Convolutional networks for biomedical image segmentation. In: MICCAI (2015)
59. Saharia, C., Chan, W., Chang, H., Lee, C.A., Ho, J., Salimans, T., Fleet, D.J., Norouzi, M.: Palette: Image-to-Image Diffusion Models. In: SIGGRAPH (2022)
60. Saharia, C., Chan, W., Saxena, S., Li, L., Whang, J., Denton, E., Ghasemipour, S.K.S., Ayan, B.K., Mahdavi, S.S., Lopes, R.G., Salimans, T., Ho, J., Fleet, D.J., Norouzi, M.: Photorealistic Text-to-Image Diffusion Models with Deep Language Understanding. In: NeurIPS (2022)
61. Saharia, C., Ho, J., Chan, W., Salimans, T., Fleet, D.J., Norouzi, M.: Image super-resolution via iterative refinement. TPAMI (2022)
62. Salimans, T., Ho, J.: Progressive distillation for fast sampling of diffusion models. arXiv (2022)
63. Saxena, S., Herrmann, C., Hur, J., Kar, A., Norouzi, M., Sun, D., Fleet, D.J.: The surprising effectiveness of diffusion models for optical flow and monocular depth estimation. arXiv (2023)
64. Saxena, S., Hur, J., Herrmann, C., Sun, D., Fleet, D.J.: Zero-shot metric depth with a field-of-view conditioned diffusion model. arXiv (2023)
65. Saxena, S., Kar, A., Norouzi, M., Fleet, D.J.: Monocular depth estimation using diffusion models. arXiv (2023)
66. Sohl-Dickstein, J., Weiss, E., Maheswaranathan, N., Ganguli, S.: Deep unsupervised learning using nonequilibrium thermodynamics. In: ICML (2015)
67. Song, S., Lichtenberg, S.P., Xiao, J.: Sun rgb-d: A rgb-d scene understanding benchmark suite. In: CVPR (2015)
68. Song, Y., Ermon, S.: Generative modeling by estimating gradients of the data distribution. arXiv (2019)
69. Song, Y., Sohl-Dickstein, J., Kingma, D.P., Kumar, A., Ermon, S., Poole, B.: Score-based generative modeling through stochastic differential equations. In: ICLR (2021)
70. Tong, A., Malkin, N., Huguette, G., Zhang, Y., Rector-Brooks, J., Fatras, K., Wolf, G., Bengio, Y.: Improving and generalizing flow-based generative models with mini-batch optimal transport. In: ICML Workshop on New Frontiers in Learning, Control, and Dynamical Systems (2023)
71. Vasiljevic, I., Kolkin, N., Zhang, S., Luo, R., Wang, H., Dai, F.Z., Daniele, A.F., Mostajabi, M., Basart, S., Walter, M.R., Shakhnarovich, G.: DIODE: A Dense Indoor and Outdoor Depth Dataset. CoRR (2019)
72. Wang, S., Saharia, C., Montgomery, C., Pont-Tuset, J., Noy, S., Pellegrini, S., Onoe, Y., Laszlo, S., Fleet, D.J., Soricut, R., Baldrige, J., Norouzi, M., Anderson, P., Chan, W.: Imagen editor and editbench: Advancing and evaluating text-guided image inpainting. arXiv (2022)
73. Wu, L., Wang, D., Gong, C., Liu, X., Xiong, Y., Ranjan, R., Krishnamoorthi, R., Chandra, V., Liu, Q.: Fast point cloud generation with straight flows. arXiv (2022)
74. Yin, W., Zhang, C., Chen, H., Cai, Z., Yu, G., Wang, K., Chen, X., Shen, C.: Metric3D: Towards zero-shot metric 3d prediction from a single image. In: ICCV (2023)
75. Yin, W., Zhang, J., Wang, O., Niklaus, S., Mai, L., Chen, S., Shen, C.: Learning to recover 3d scene shape from a single image. In: CVPR (2021)

76. Yu, Z., Peng, S., Niemeyer, M., Sattler, T., Geiger, A.: Monosdf: Exploring monocular geometric cues for neural implicit surface reconstruction. *NeurIPS* (2022)
77. Yuan, W., Gu, X., Dai, Z., Zhu, S., Tan, P.: New crfs: Neural window fully-connected crfs for monocular depth estimation. *arXiv* (2022)
78. Zhang, C., Yin, W., Wang, B., Yu, G., Fu, B., Shen, C.: Hierarchical normalization for robust monocular depth estimation. *NeurIPS* **35** (2022)
79. Zhang, L., Rao, A., Agrawala, M.: Adding conditional control to text-to-image diffusion models. In: *ICCV* (2023)
80. Zhang, Y., Guo, X., Poggi, M., Zhu, Z., Huang, G., Mattoccia, S.: Completion-former: Depth completion with convolutions and vision transformers. In: *Proceedings of the IEEE/CVF Conference on Computer Vision and Pattern Recognition*. pp. 18527–18536 (2023)
81. Zhao, W., Rao, Y., Liu, Z., Liu, B., Zhou, J., Lu, J.: Unleashing text-to-image diffusion models for visual perception. *arXiv* (2023)

A Appendix for DepthFM: Fast Monocular Depth Estimation with Realistic Geometry using Flow Matching

A.1 Additional Qualitative Comparison

Fig. 12 and Fig. 13 show additional qualitative comparisons with other state-of-the-art monocular depth estimation methods. Images and predictions for the other models are taken from [64]. For both, indoor and outdoor scenes, our model consistently produces depth maps with higher fidelity than the other methods. Our method particularly excels in outdoor scenes, showing a clear distinction between objects in the far distance and the sky, especially visible in the samples from DIODE, KITTI, and virtual KITTI 2 in Fig. 13. ZoeDepth [5] and DMD [64] fail to distinguish objects that are further away.

Indoor scenes in Fig. 12 are from DIODE [71], Hypersim [56], ibims-1 [36], NYU-v2 [46], and SunRGBD [67]. Outdoor scenes in Fig. 13 are from DDAD [22], DIML [10], DIODE [71], KITTI [21], and virtual KITTI 2 [7].

A.2 Further Applications

Video Depth Estimation Fig. 14 shows our DepthFM model applied on a video. We estimate the depth with 5 ensemble members and two ODE steps. Since our model predicts relative depth we scale and shift the current frame based on the depth of the previous frame to ensure temporal consistency.

Conditional Synthesis Fig. 15 shows a comparison of depth-conditioned synthesis results. We first infer depth based on an image using our DepthFM and the ZoeDepth [5] model, and then use a pre-trained depth-to-image ControlNet [79] with Stable Diffusion 1.5 to synthesize new samples based on the depth maps and a text prompt. We can clearly observe that the depth maps obtained with ZoeDepth do not reflect the actual depth well and additionally are inaccurate for some parts of the image. In contrast, our method yields sharp and realistic depth maps. This result is also reflected in the synthesized results, where images created based on our depth map more closely resemble the actual image.

Generation of 3D Pointclouds Using our monocular depth-estimate d inferred from a sparse depth, we can generate a 3D point cloud via back-projection. Specifically, for a 2d-point x (in homogeneous coordinates), we map it to a 3D-point y using the intrinsic camera-matrix K via the relation $y = d \cdot K^{-1}x$. A few samples are shown in Fig. 20. For details regarding the depth-completion model, see section 4.3.

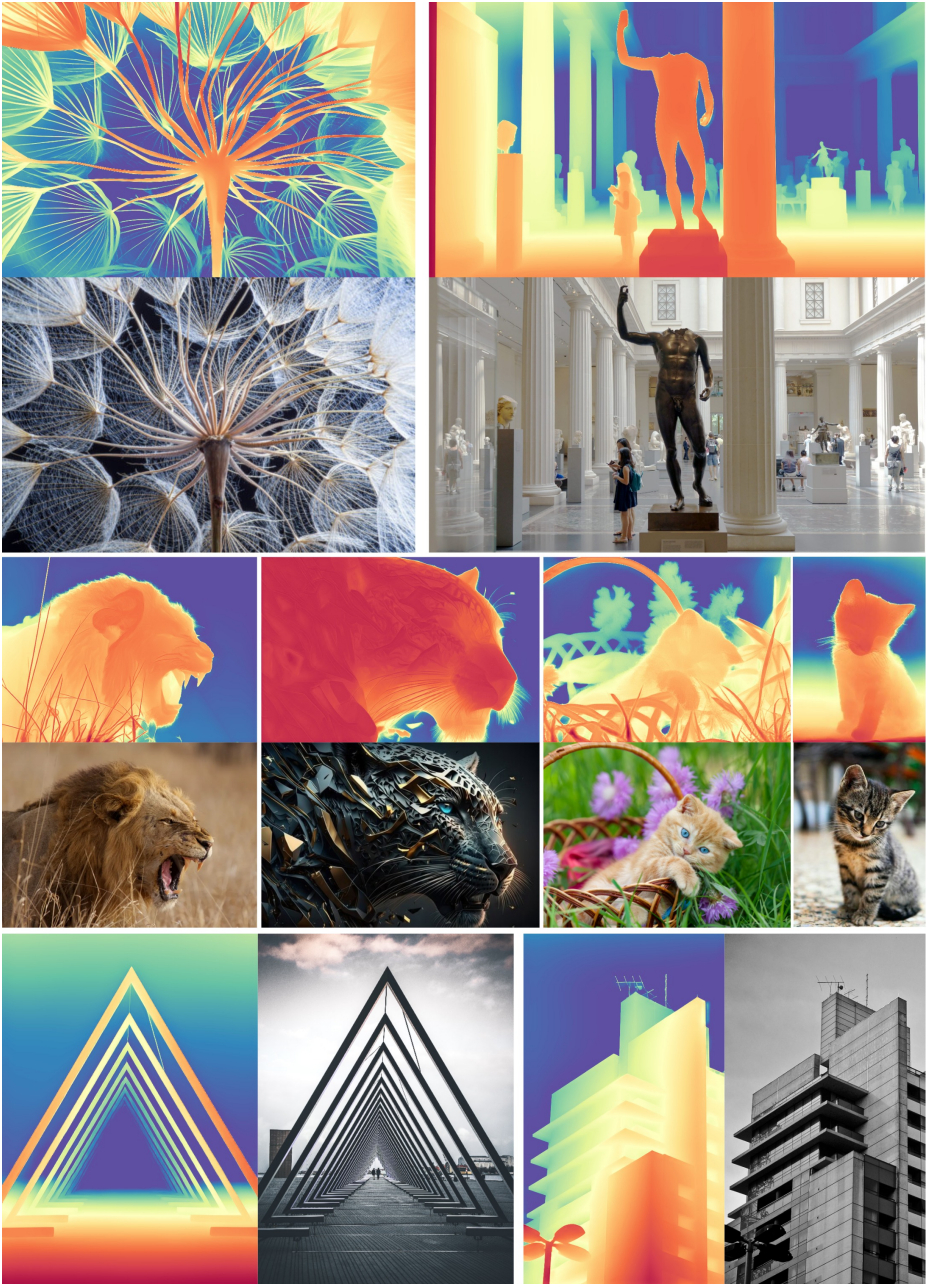


Fig. 11: Generalization to real-world data with varying resolutions and aspect ratios. Best viewed when zoomed in.

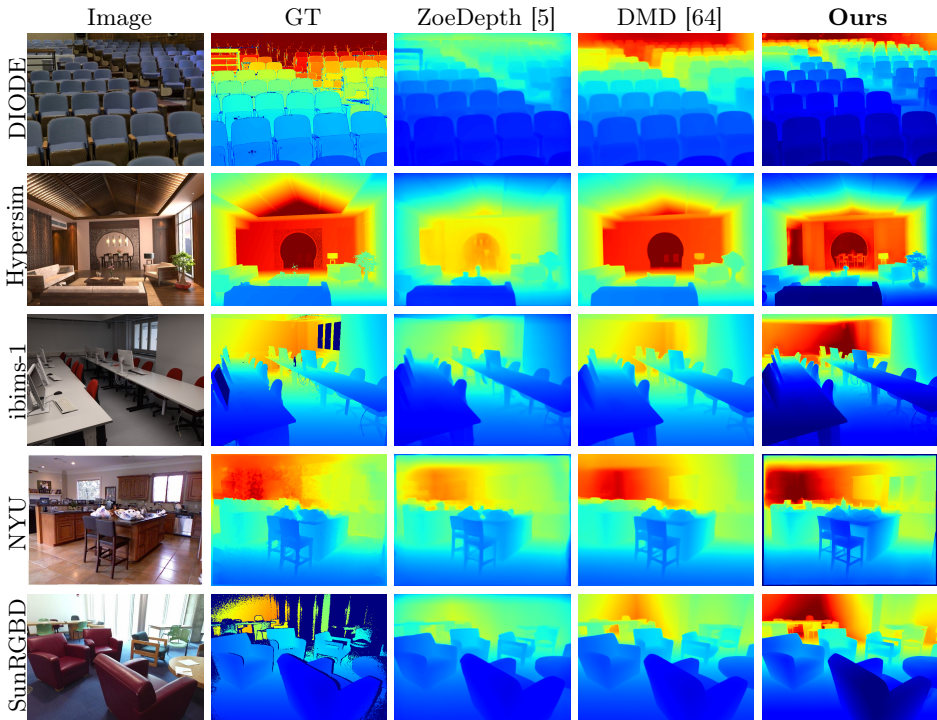


Fig. 12: Indoor scenes comparison. Best viewed when zoomed in.

A.3 Additional Ablations

Data Preprocessing The pre-trained autoencoder of Latent Diffusion Models [57] expects the input data to be within the range $[-1, 1]$. To reach this range, we ablate two normalization techniques. First, linear normalization, which linearly normalizes the values at the 2%- and 98%-percentiles. Second, is log normalization, which shifts the percentile normalization to log space. The raw depth and the correspondingly normalized distributions are visualized in Fig. 16. In particular, linear normalization allocates limited representational capacity to indoor scenes, whereas log-scaled depth allocation alleviates the problem and allocates similar capacity to both, indoor and outdoor scenes. We also observe empirical benefits from log scaling, as shown in Tab. 5.

It is worth noting that some of the depth data, including the synthetic data that we train our models on, contains invalid values due to e.g., infinite distance or the absence of valid scene geometry at certain pixels. We compute the invalid mask from the depth maps and resize it to accommodate the smaller latent space. We then threshold the small invalid depth map to map all values below 1 to ensure that we get only valid ground truth depth maps within the mask. The invalid values are interpolated using nearest neighbors and then passed to the encoder to ensure compatibility with a valid latent representation.

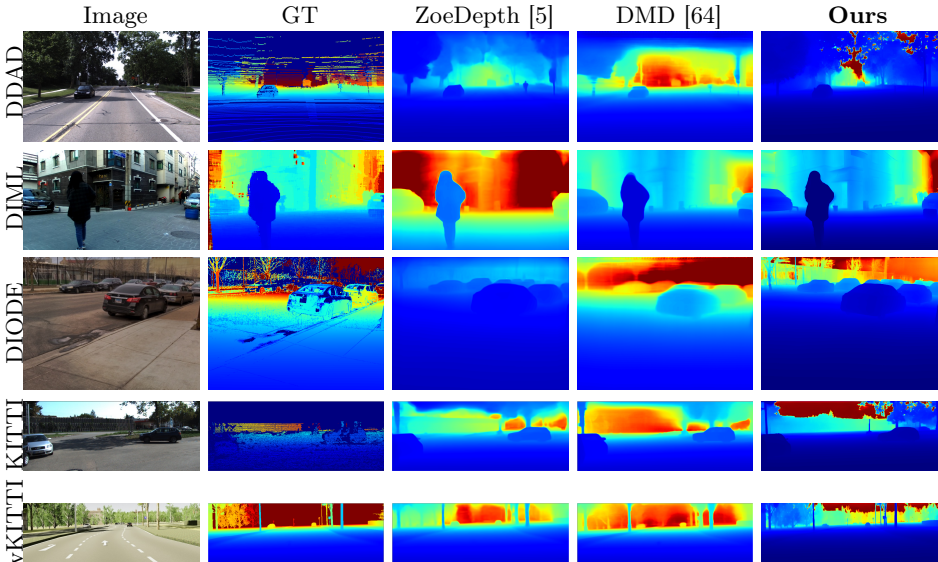


Fig. 13: Outdoor scenes comparison. Best viewed when zoomed in.

Table 5: Ablation of the data normalization strategy.

Transform	NYU-v2 [46]		DIODE [71]	
	AbsRel↓	$\delta 1 \uparrow$	AbsRel↓	$\delta 1 \uparrow$
Identity	0.080	93.92	0.237	78.77
Log	0.069	95.22	0.227	79.76

Training Data Similarly to *Marigold* [35] we train our model on the synthetic Hypersim [56] and virtual KITTI [7] datasets. Fig. 17 shows the zero-shot performance comparison on the KITTI dataset between two models: one trained solely on the indoor Hypersim dataset and another trained on a combination of both datasets. The results clearly show that the integration of v-KITTI into the training process improves the inference accuracy for outdoor scenes, providing realistic depth estimates even for distant objects.

A.4 Training Details

For all of the training runs, we finetune from the SD2.1 checkpoint. Consequently, we keep the network UNet architecture fixed except for the first convolutional layer to incorporate the extra image conditioning. We duplicate channel-wise the weights of the first convolutional layer and scale them appropriately to ensure that the input to the subsequent layer remains within a reasonable range.

We employ a global batch size of 128, a learning rate of 3×10^{-5} , and an EMA rate of 0.999.

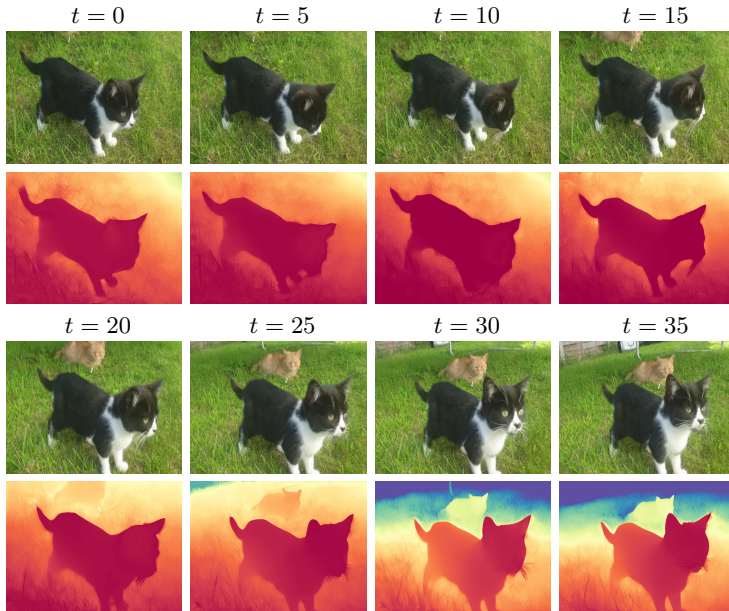


Fig. 14: Video depth prediction with our DepthFM model.

A.5 Normal Estimation from Depth

To estimate the normals from a given depth, we chose the simple LINE-MOD-SNE [17,25]. We follow the notation from [17]. This normal-estimator works, by estimating a 3d-plane using the depth, and finally computing the normal to this surface. Let $\tilde{p}_i = [u_i, v_i]^\top$ be an arbitrary pixel. For the depth d we compute the gradient $\nabla d = [\partial d/\partial u, \partial d/\partial v]^\top$ and form a 3D-plane with the points

$$p_0 = t(\tilde{p}_i)d \quad (9)$$

$$p_1 = t(\tilde{p}_i + [1, 0]^\top) \left(d + \frac{\partial d}{\partial u} \right) \quad (10)$$

$$p_2 = t(\tilde{p}_i + [0, 1]^\top) \left(d + \frac{\partial d}{\partial v} \right) \quad (11)$$

This computation requires the focal length of the camera, which is readily available in the Hypersim-dataset [56]. Finally, the surface-normal at \tilde{p}_i is estimated as

$$n_i = \frac{(p_1 - p_0) \times (p_1 - p_2)}{\|(p_1 - p_0) \times (p_1 - p_2)\|_2} \quad (12)$$

Note that this computation is differentiable with respect to the input, and can therefore be used in backpropagation.

Modeling Confidence As mentioned in [17], the error of the normal-estimator in Eq. (12) is concentrated at the edges of the image. Therefore, to filter out these

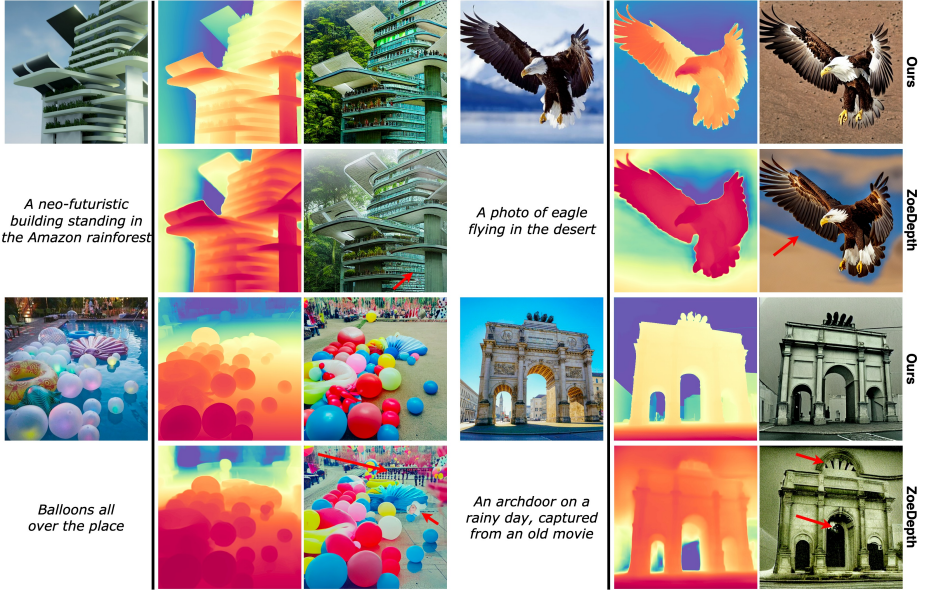


Fig. 15: The superior and high-fidelity depth map generation capability of DepthFM also empowers ControlNet [79] to generate images with depth fields that closely mimic the source image in a zero-shot manner. ZoeDepth [5] fails to replicate the exact depth field, as evidenced by the discrepancy between the corresponding ControlNet output and the source images, highlighted by the red arrows. The prompts for ControlNet are visualized in the lower left corners, and the images are generated using the same random seed. Best viewed when zoomed in.

edges of our estimated normal, we first compute the edges via a Sobel filter $F_S(\hat{d})$. The final binary mask then consists of the pixels, which are a certain distance from these edges. We simply implement this by checking $F_S(\hat{d}) > \tau$ for a threshold τ per-pixel, yielding a binary mask $\mathcal{M}_\tau = \mathcal{M}$. Depending on the choice of τ , a certain number of pixels is filtered out. This is visualized in Fig. 18. For the training on Hypersim, we chose $\tau = 2$.

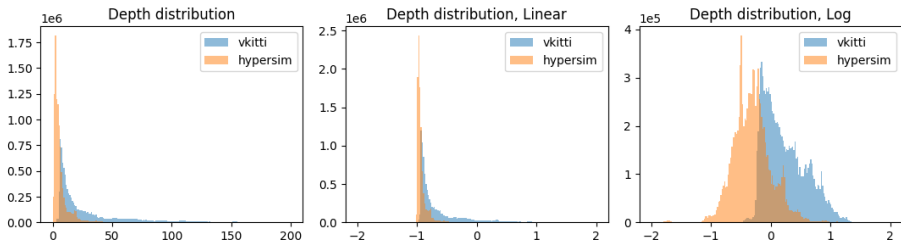


Fig. 16: The distribution of the raw metric depth, and the sample distribution after different normalization techniques.

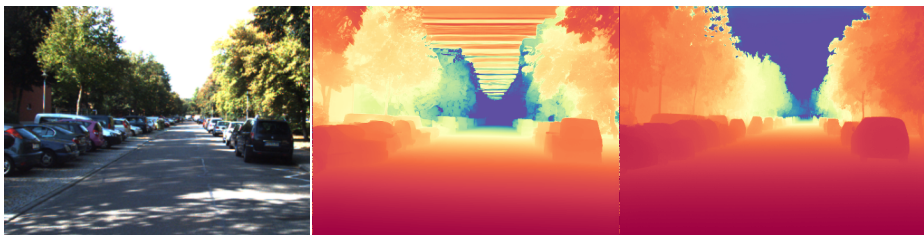


Fig. 17: Comparison of zero-shot depth estimation on the KITTI dataset. The left image is the groundtruth image, the middle one showcases the model trained only on Hypersim, and the right image displays the model trained on a combination of Hypersim and VirtualKitti. This comparison underscores the extra value of incorporating virtual outdoor training data for improved performance in outdoor scenes.

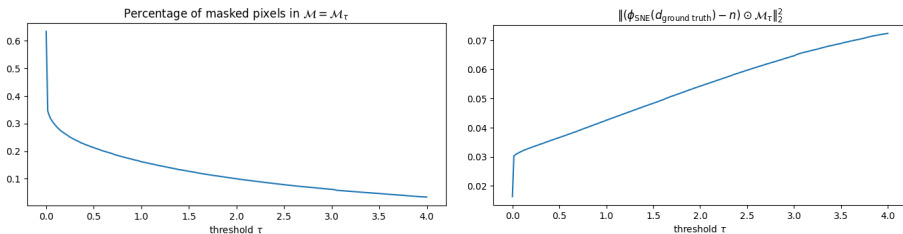


Fig. 18: Visualization of the choice of τ in Hypersim [56]: Depending on the choice of τ , we observe a tradeoff between the number of pixels we discard and the magnitude of the error.

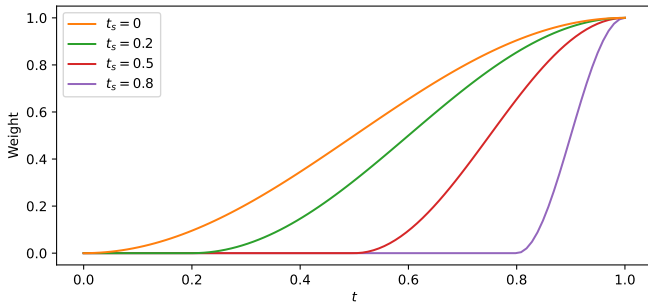


Fig. 19: Cosine weighting function of surface normals loss for different starting t . We empirically find $t_s = 0.2$ to work best.



Fig. 20: Pointclouds generated from a given sparse depth. We first generate a monocular depth-estimate d from a given sparse depth, which in turn can be used to produce a pointcloud.